



Mathematical modelling of a membrane-less redox flow battery based on immiscible electrolytes

Désirée Ruiz-Martín^a, Daniel Moreno-Boza^a, Rebeca Marcilla^b, Marcos Vera^a,
Mario Sánchez-Sanz^{a,*}

^a Departamento de Ingeniería Térmica y de Fluidos, Universidad Carlos III de Madrid, Leganés, 28911, Madrid, Spain

^b Electrochemical Processes Unit, IMDEA Energy, Avda. Ramón de la Sagra 3, Móstoles 28935, Madrid, Spain

ARTICLE INFO

Article history:

Received 14 April 2021

Revised 24 July 2021

Accepted 14 August 2021

Available online 25 August 2021

Keywords:

Membrane-less redox flow battery

Immiscible electrolyte

Interface instability

Dilute solutions

ABSTRACT

We present a mathematical model to study the steady-state performance of a membrane-less reversible redox flow battery formed by two immiscible electrolytes that spontaneously form a liquid-liquid system separated by a well defined interface. The model assumes a two-dimensional battery with two coflowing electrolytes and flat electrodes at the channel walls. In this configuration, the analysis of the far downstream solution indicates that the interface remains stable in all the parameter range covered by this study. To simplify the description of the problem, we use the dilute solution theory to decouple the calculation of the velocity and species concentration fields. Once the velocity field is known, we obtain the distribution of the mobile ionic species along with the current and the electric potential field of the flowing electrolyte solution. The numerical integration of the problem provides the variation of the battery current density I_{app} with the State of Charge (SoC) for different applied cell voltages V_{cell} . A detailed analysis of the concentration density plots indicates that the normal operation of the battery is interrupted when reactant depletion is achieved near the negative electrode both during charge and discharge. The effect of the electrolyte flow on the performance of the system is studied by varying the Reynolds, Re , and Péclet, Pe , numbers. As expected, the flow velocity only affects the polarization curve in the concentration polarization region, when V_{cell} is well below the equilibrium potential, resulting in limiting current densities that grow with Re as $j_{lim} \sim Re^{0.3}$. In addition, both the single-pass conversion efficiency ψ and the product ψj_{lim} decrease with Re . Concerning the later, the decay rate with Re exhibits a power law with an exponent that almost doubles previous theoretical predictions obtained by imposing a prescribed velocity profile for the electrolyte in a membrane-less laminar flow battery with a liquid oxidant and gaseous fuel. The present work constitutes the first modelling attempt that simultaneously solves the fluid dynamical system formed by the two immiscible electrolytes and the electrochemical problem that determines the response of the membrane-less battery. The proposed model could be used as a valuable tool to optimize future flow battery designs based on immiscible electrolytes.

© 2021 The Authors. Published by Elsevier Inc.

This is an open access article under the CC BY-NC-ND license
(<http://creativecommons.org/licenses/by-nc-nd/4.0/>)

* Corresponding author.

E-mail address: mssanz@ing.uc3m.es (M. Sánchez-Sanz).

1. Introduction

The intermittent nature of energy production from renewable energy sources such as wind or solar demands extensive energy-storage systems. A well established technology to store the energy generated in stationary applications are electrochemical storage technologies such as rechargeable batteries, where the electricity is stored in chemicals to be later released upon demand [1]. Redox Flow Batteries (RFBs) present several advantages over conventional batteries, namely, total decoupling of power and energy, flexible modular design and operation, excellent scalability and long-life cycling[2].

The major issues of the state-of-the-art vanadium RFBs are the high price, scarcity and potential toxicity of vanadium electrolytes and the high cost and low performance of the ion-selective membranes required to separate the anolyte from the catholyte. The current limitations of vanadium based electrolytes [3] have encouraged their substitution by organic redox couples that are cheaper, more abundant and environmentally friendly [4]. Unfortunately, regardless of the nature of the electrolytes, most RFBs rely on the use of expensive ion-selective membranes (40% of the total cost [5]) that separate the two active electrolytes while facilitating the exchange of the charge carriers. To reduce this cost, a current trend seeks to remove the expensive membranes by using immiscible electrolytes in which the interface separating the catholyte and anolyte allows the exchange of active species [6]. Navalpotro et al. [4] demonstrated that an acidic solution and a hydrophobic ionic liquid, both containing dissolved quinoyl species, can be used to form a system that behaves as a battery without a membrane, achieving a power density of 1.98 mW/cm² [7]. Also, Bamgboya et al. [8] built a RFB based on immiscible, organic, all-iron liquid electrolytes to achieve a peak power density of 0.7 mW/cm². Different combinations of immiscible redox electrolytes have been later tested to improve the system power density up to 3 mW/cm² for nonaqueous-aqueous immiscible electrolytes [9] and up to 23 mW/cm² for aqueous-aqueous biphasic systems [10].

Some of the main challenges of membrane-less RFB are the low current densities achieved, enhanced crossover or cross-contamination, self-discharge at the interface or electrolyte mixing due to diffusion or gravity-induced mixing [2]. Among the potential problems we add here, as we will show later in Section 2, mixing of the electrolytes as a consequence of flow instabilities at large Reynolds numbers.

It is important to mention that in most reported examples of membrane-less RFBs based on immiscible electrolytes all the electrochemical tests were done under static conditions. Experiments under flow are scarce in the literature. Also, most reactors used in RFBs are not valid to test this membraneless-concept due to the zero-gap configuration of filter-press reactors. An example of analysis of the effect of the inter-electrode gap on the cell potential can be found in [11]. Therefore, new reactor designs that allow the formation of the two phases within the reactor are needed to validate the concept under flowing conditions. In this scenario, multiphysics fluid-dynamic/electrochemical models might help to accelerate the development of proper reactor designs to demonstrate the membrane-less concept under flowing conditions.

Unlike previous modelling efforts of membrane-less RFBs that either used a prescribed velocity profile for the electrolytes [12–14] or considered only one fluid phase [15,16], the model presented here includes for the first time a full analysis of both the fluid dynamical and electrochemical aspects of a membrane-less RFB with immiscible electrolytes. To this end, we assume the limit of very dilute solutions in order to decouple the calculation of the flow field from the electrochemical problem that determines the species concentration field. This enables an *a priori* analysis of the stability of the interface separating the two electrolytes, which must remain stable for the flow battery to be operated in a controllable manner.

As model configuration, we shall consider a slender two-dimensional (2D) channel of width h and length $L \gg h$, fed with two liquid electrolyte solutions with flow rates per unit of length Q_1 and Q_2 , as sketched in Fig. 1. The results presented in the manuscript correspond to a channel height of the order of $h = 1$ cm and a length of the cell $L = 10$ cm. These values are

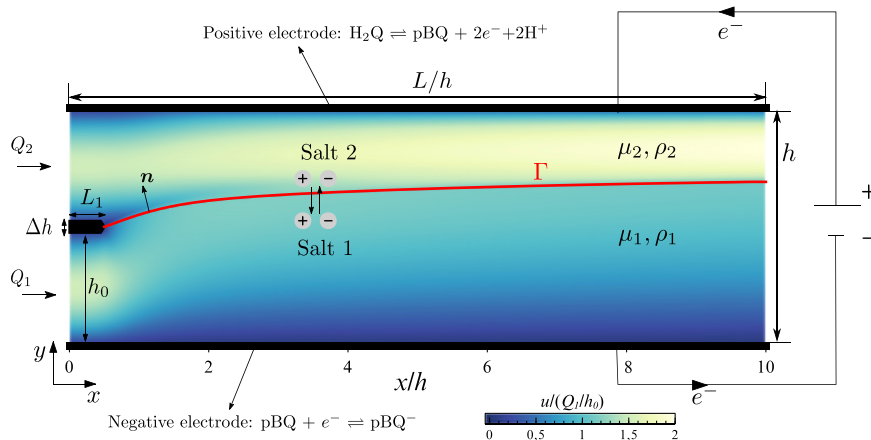


Fig. 1. Schematics of the problem, including the geometrical, fluid-dynamical, and electrochemical relevant parameters. The figure includes a sample calculation of the velocity field obtained for $Q_2/Q_1 = 1, \mu_2/\mu_1 = 0.0125, Re = 10$ and the geometrical parameters included in Table 1. The thick red curve indicates the location of the interface Γ that separates the immiscible electrolytes.

Table 1
Fluid and geometrical parameters.

	Parameter	Value
Reynolds Number	$Re = \rho_1 \bar{u}_1 h_0 / \mu_1$	$0 < Re < 20$
Volumetric flow rate ratio	Q_2 / Q_1	1
Density ratio	ρ_2 / ρ_1	1
Viscosity ratio	μ_2 / μ_1	0.0125
Geometrical parameters	h_0 / h	0.49
	$H = (h_0 + \Delta h) / h$	0.51
	L / h	10
	L_1 / h	0.5

similar to the dimensions of the proof-of-concept experimental battery (separation of the electrodes $h \simeq 2$ cm and length $L \simeq 16$ cm) developed by [4]. Notice that the slenderness L/h of the numerical model is slightly larger than the slenderness of the experimental device to ensure a one-directional two-layer Poiseuille flow at the outlet of the computational domain. Both fluids, assumed to have constant density and viscosity, ρ_i and μ_i ($i = 1, 2$), are initially separated at the channel entrance by a thin splitter plate of thickness $\Delta h \ll h$ and length $L_1 \ll L$, located at a distance $h_0 \sim h$ from the lower wall. To compute the velocity and pressure fields within the fluid domain we use the Navier-Stokes equations together with the Arbitrary Lagrangian-Eulerian method to track the location of the interface separating both fluids as a function of the governing dimensionless parameters: viscosity, density and flow rate ratios, μ_2/μ_1 , ρ_2/ρ_1 and Q_2/Q_1 , respectively, Reynolds number, $Re = \rho_1 Q_1 / \mu_1$, channel slenderness, h/L , and splitter-plate position, h_0/h .

The electrochemical cell under study is based on the flow of two immiscible liquid electrolytes between two metal flat electrodes, as shown in Fig. 1. Following Navalpotro et al. [4] we consider organic molecules instead of vanadium compounds, because of its abundance and lower toxicity and price. In particular, fluid 2 consists of an acidic solution of hydroquinone (H_2Q) while fluid 1 consists of the redox-active organic molecule parabenzoquinone (pBQ) dissolved in a hydrophobic liquid, either propylene carbonate (PC) or 1-butyl-1-methylpyrrolidinium bis(trifluoro-methanesulfonyl)imide (PYR₁₄TFSI). In the latter case we assume that the solution is neutral to ensure the validity of dilute solution theory. Also, following [4], we consider that the concentration of the supporting electrolyte is much greater than the molar concentration of the active species and the concentration of protons will basically remain constant, leaving the acidity of the catholyte unchanged.

The half-cell redox reactions at the positive (fluid 2) and negative (fluid 1) electrodes are given in Eqs. (1) and (2), respectively.



During charge, hydroquinone (H_2Q) in acidic media suffers a reversible oxidation to parabenzoquinone (pBQ) in one step, involving the exchange of 2 electrons and 2 protons whereas the parabenzoquinone (pBQ) in aprotic electrolyte undergoes a two consecutive reversible reduction reactions to radical anion (pBQ^-) and dianion (pBQ^{2-}), exchanging 2 electrons in total. However, the second reduction step was not observed experimentally during battery operation [4,10] so only the first reaction was considered here.

2. The fluid mechanics problem

As previously discussed, in the limit of very dilute solutions the velocity and concentration fields are decoupled and can be analysed independently. We shall therefore start studying the flow of two immiscible incompressible Newtonian fluids, with equal densities $\rho_1 = \rho_2$ and different viscosities, μ_1 and μ_2 , through the two-dimensional channel presented in Fig. 1. The position of the interface Γ separating the two fluids is initially unknown and must be calculated as part of the solution.

The fluid dynamics is governed by the Navier-Stokes equations

$$\nabla \cdot \mathbf{v}_i = 0, \quad \rho_i \frac{D\mathbf{v}_i}{Dt} = \nabla \cdot \mathbf{T}_i, \quad \mathbf{x} \in \Omega_i, \quad i = 1, 2 \tag{3}$$

in each fluid domain Ω_i . In these equations $\mathbf{x} = (x, y)$ is the position vector in two-dimensional Cartesian coordinates, t is time, and $\mathbf{T}_i = -p_i \mathbf{I} + \mu_i (\nabla \mathbf{v}_i + \nabla \mathbf{v}_i^T)$ is the stress tensor, with p and $\mathbf{v} = (u, v)$ denoting the pressure and velocity fields, respectively, and $D/Dt = \partial/\partial t + \mathbf{v}_i \cdot \nabla$ is the substantial derivative.

2.1. Initial and boundary conditions

Keeping in mind that our goal is to study the steady-state performance of the battery, we use a transient method to compute the steady velocity field \mathbf{v} and the location of the interface Γ . Therefore, the system of equations defined in (3) must

be supplemented with the appropriate initial and boundary conditions to be discussed below. At $t = 0$, the flow is assumed to be at rest, i.e., $u = v = 0$ everywhere in the computational domain, except at $x = 0$, where we impose $v = 0$ and a streamwise velocity u corresponding to fully developed laminar flows in each electrolyte, with respective volume flow rates $Q_1 = \int_0^{h_0} u \, dy$ and $Q_2 = \int_{h_0+\Delta h}^h u \, dy$, such that

$$\begin{aligned} \frac{u}{\bar{u}_1} &= \frac{6}{h_0} \frac{h}{h} \left[\frac{y}{h} - \left(\frac{y}{h} \right)^2 \frac{h}{h_0} \right], & 0 < y < h_0, \\ \frac{u}{\bar{u}_1} &= \frac{Q_2}{Q_1} \frac{6h_0}{h} \frac{1}{(1-H)^3} \left[(1+H) \frac{y}{h} - \left(\frac{y}{h} \right)^2 - H \right], & h_0 + \Delta h < y < h, \end{aligned}$$

with $H = (h_0 + \Delta h)/h$ and $\bar{u}_1 = Q_1/h_0$ the average velocity of fluid 1. A homogeneous natural boundary condition $\mathbf{T} \cdot \mathbf{n} = 0$ is imposed at $x = L$, with \mathbf{n} denoting the outward unit normal vector at the outflow boundary of the domain, while non-slip conditions $u = v = 0$ are imposed at the wall surfaces.

At the fluid-fluid interface $y = \Gamma(x, t)$ continuity of velocities and the jump condition on the stress tensor are enforced

$$\mathbf{v}_1 = \mathbf{v}_2, \tag{4}$$

$$\mathbf{n} \cdot (\mathbf{T}_1 - \mathbf{T}_2) = \sigma \mathbf{n} \nabla \cdot \mathbf{n}, \tag{5}$$

where \mathbf{n} represents the unit vector normal to the surface Γ pointing towards the more viscous fluid and σ is the surface tension, that we consider negligible in all calculations below $\sigma = 0$. We describe the interface using the implicit equation $f(x, y, t) = \Gamma(x, t) - y = 0$. Because $f = 0$ on the interface at all times, the material derivative must satisfy

$$\frac{\partial f}{\partial t} + \mathbf{v}_i \cdot \nabla f = 0, \tag{6}$$

where \mathbf{v}_i denotes the velocity of the interface.

2.2. Numerical method

The system of equations described above is integrated using the finite element method for the spatial discretization using the software COMSOL Multiphysics [17]. Equations (3) are written in weak form

$$\int_V \left[\tilde{p} \nabla \cdot \mathbf{v} + \rho \frac{D\tilde{\mathbf{v}}}{Dt} \cdot \tilde{\mathbf{v}} - \tilde{p} \nabla \cdot \tilde{\mathbf{v}} + \mu (\nabla \mathbf{v} + \nabla \mathbf{v}^T) : \nabla \tilde{\mathbf{v}} \right] dV = 0, \tag{7}$$

where \tilde{p} and $\tilde{\mathbf{v}}$ are the test functions for pressure and velocity, respectively. Unstructured quadrilateral meshes with Taylor-Hood elements are used to discretize Eqs. (3) for pressure and velocity. Near the center of the channel, the size of the elements reached the maximum value $\Delta \xi/h = 3 \times 10^{-2}$ and was reduced near the walls, where we clustered the elements to reach the minimum element size $\Delta \xi/h = 3 \times 10^{-3}$ and a total of $n_0 = 11638$ elements. To check the independence of the results with the grid, we monitored the position of the interface Γ at $x/L = 1$ reducing, progressively, the maximum element size to increase the density of the mesh n , giving $\Gamma/h = (0.7146, 0.7141, 0.7139, 0.7139, 0.7139)$ for $n/n_0 = (0.27, 0.44, 0.67, 1, 1.79)$. The value $n = n_0$ with minimum element size $\Delta \xi/h = 0.003$ was maintained in all the results shown below. Keeping the number of elements n within the range indicated above, we checked that the grid did not affect the results by comparing non-uniform meshes with different distributions.

The fluid-fluid interface Γ is tracked using the Arbitrary Lagrangian-Eulerian (ALE) technique [18], which enables to impose the kinematic boundary condition (6) along the interface by prescribing the normal velocity of the mesh. When the viscosity ratio μ_2/μ_1 is close to unity, the displacement of the mesh elements is computed by solving a Laplace equation for the displacement field, namely $\nabla^2 \mathbf{q} = 0$, $\mathbf{q} = (q_x, q_y)$, with suitable boundary conditions. To ensure convergence with small viscosity ratios $\mu_2/\mu_1 \ll 1$, a minimum mesh deformation energy strategy was applied in this case for the computation of the mesh displacement.

The temporal discretization of the system of nonlinear partial differential equations is carried out using a second-order variable-step BDF method. At every time step, an iterative Newton method is used to solve the algebraic system of equations that continues until the weighted Euclidean norm of the error vector falls below 10^{-6} . As mentioned above, the initial conditions corresponded to a quiescent state $u = v = 0$ with the interface located at $\Gamma = h_0 + \Delta h/2$. The time-dependent solver was complemented with an automatic remeshing algorithm that redistributed the mesh elements along the curved interface Γ .

The numerical method has been extensively verified in Appendix A by comparing in Fig. A.10 the computational results with the asymptotic solution achieved for $x/L \gg 1$ in the limit of quasi one-directional flow $Re h/L \ll 1$. The largest Reynolds number considered in this study satisfies $Re \leq Re_c \approx 27$, where Re_c represents the critical Reynolds above which we find shear-flow instabilities in the less viscous fluid [19] at $x = 0$. Below the above mentioned Reynolds number, the discontinuity in the shear rate resulting from the viscosity jump at the interface initiates Yih's instability [20]. The absolute or convective nature of this instability, of relevance in order to anticipate the fluid dynamical behaviour of the battery, depends strongly on the viscosity ratio μ_2/μ_1 and surface tension σ . The stability analysis included in Appendix A addresses

Table 2

Electrochemical parameters of the species in the positive electrode for the battery model obtained from [4], except D_{H^+} [29].

Symbol	Parameter	Value
D_{H_2Q}	H ₂ Q diffusion coefficient	$4.10 \times 10^{-8} \text{ m}^2/\text{s}$
D_{pBQ}	pBQ diffusion coefficient	$4.10 \times 10^{-8} \text{ m}^2/\text{s}$
D_{H^+}	H ⁺ diffusion coefficient	$9.33 \times 10^{-9} \text{ m}^2/\text{s}$
$K_{H_2Q}^0$	H ₂ Q standard rate constant	$73.17 \times (1, 10^{-3}) \text{ Am/mol}$
α_f, α_b	Transfer coefficients	0.5
$c_{H_2Q}^0$	Initial concentration of H ₂ Q	10 mM
$c_{H^+}^0$	Initial concentration of H ⁺	100 mM

Table 3

Electrochemical parameters of the species in the negative electrode for the battery model obtained from [4], except D_{H^+} [30] [31].

Symbol	Parameter	Value
D_{pBQ}	pBQ diffusion coefficient	$5.80 \times 10^{-9} \text{ m}^2/\text{s}$
D_{pBQ^-}	pBQ ⁻ diffusion coefficient	$8.64 \times 10^{-8} \text{ m}^2/\text{s}$
D_{H^+}	H ⁺ diffusion coefficient	$3.0 \times 10^{-9} \text{ m}^2/\text{s}$
K_{pBQ}^0	pBQ standard rate constant	$0.11 \times (1, 10^{-3}) \text{ Am/mol}$
α_f, α_b	Transfer coefficients	0.5
c_{pBQ}^0	Initial concentration of pBQ	20 mM

the worst case scenario $\sigma = 0$, showing that a small perturbation in the flow that deforms the interface results in a perturbation wave whose amplitude grows as it is convected downstream. Nevertheless, as can be seen in Fig. A.12, for the range of flow parameters considered in this work (Table 1), this effect is temporary and the interface recovers its initial shape once the perturbation has disappeared. In brief, the convective nature of the instability ensures the validity of the steady electrochemical analysis to be presented in the following sections.

3. The electrochemical problem

Numerical integration of the fluid mechanical problem stated above with the flow parameters Q_2/Q_1 , μ_2/μ_1 and Re specified in Table 1 provides the steady-state velocity field \mathbf{v} and the location of the interface Γ . The spatial distribution of the concentrations of active species is obtained in a second step by integrating the mass conservation equation for all species participating in the positive and negative electrode redox reactions, as described in Eqs. (1) and (2). The mass conservation equation for species $j = 1, \dots, N$ takes the form [21]

$$\frac{\partial c_j}{\partial t} + \nabla \cdot \mathbf{N}_j = 0, \tag{8}$$

with c_j the molar concentration. In the limit of dilute solutions, the molar flux of the j -th species, \mathbf{N}_j , is driven by convection, diffusion and migration, according to

$$\mathbf{N}_j = \mathbf{v}c_j - D_j \nabla c_j - \zeta_j z_j F c_j \nabla \phi_i, \tag{9}$$

where ϕ_i is the electrostatic or ionic potential, F is Faraday’s constant and z_j is the charge number of the species j . In writing Eq. 9, we assumed that the activity coefficients are close to unity as a consequence of the dilute solution hypothesis ([22], page 95). The electrochemical mobility is given by the Nernst-Einstein equation $\zeta_j = D_j/RT$, with D_j the mass diffusion coefficient of species j , T the temperature and R the universal gas constant. The interface Γ separating the two immiscible electrolytes is permeable to mobile species. The diffusion coefficient D_j of the species depends on the electrolyte in which they are present and, similarly to the electrolyte density and viscosity, is defined as $D_j = D_{j,1}$ for $f > 0$ (fluid 1) and $D_j = D_{j,2}$ for $f < 0$ (fluid 2), being $D_{j,1}$ and $D_{j,2}$ the diffusion coefficient of the species j in the anolyte, $y < \Gamma$, and catholyte, $y > \Gamma$, respectively (see tables 2 and 3 for the values used in this study).

The motion of charged species through the fluid induces a current that can be computed based on the molar flux according to

$$\mathbf{i} = F\mathbf{v} \sum_{j=1}^N z_j c_j - F \sum_{j=1}^N z_j D_j \nabla c_j - \kappa \nabla \phi_i, \tag{10}$$

where $\kappa = F^2 \sum_{j=1}^N z_j^2 \zeta_j c_j$ denotes the electrical conductivity of the solution. Hereafter, the sums run over $j = 1, \dots, N$ unless stated otherwise.

In aqueous electrochemical solutions and in a large fraction of non-aqueous electrolytes, the condition of electroneutrality $\sum z_j c_j = 0$ holds closely everywhere. Note that although this condition is not satisfied in the Debye layers formed near the charged boundaries, the influence of these layers is negligible due to their small characteristic thickness [23] and can be

neglected in first approximation. In this case, the first term in the right hand side of Eq. (10) vanishes and, in the absence of charge accumulation $\nabla \cdot \mathbf{i} = 0$, the electric potential ϕ_i is computed by solving

$$\nabla \cdot \mathbf{i} = \nabla \cdot \left(-\kappa \nabla \phi_i - F \sum z_j D_j \nabla c_j \right) = 0 \tag{11}$$

instead of using Poisson's equation [21].

3.1. Electrode kinetics

Assuming one-step electrochemical reactions, the dependence of the electrode current density j on the overpotential η and on the active species concentrations at the electrode surface c_R and c_O is modelled using the Butler-Volmer equation [24,25]

$$\frac{j}{j_0} = \frac{c_R}{c_R^*} \exp \left(\frac{(1-\alpha)n_e F}{RT} \eta \right) - \frac{c_O}{c_O^*} \exp \left(-\frac{\alpha n_e F}{RT} \eta \right), \tag{12}$$

where α is the transfer coefficient, which quantifies the ratio between the forward and backward reaction rates for a given applied potential, and n_e is the number of electrons transferred in the overall reaction. Equation (12) holds for both electrodes, the subscripts O and R representing the oxidized and reduced species in the redox reaction taking place on each electrode. Thus, at the positive electrode we have $c_O = c_{\text{pBQ}}$ and $c_R = c_{\text{H}_2\text{Q}}$, while at the negative electrode $c_O = c_{\text{pBQ}}$ and $c_R = c_{\text{pBQ}^-}$. The superscript * is used for the reference values on the bulk fluid. In the Butler-Volmer equation, $j_0 = K^0 c_O^{*(1-\alpha)} c_R^{*\alpha}$ denotes the exchange current density, the rate at which the anodic and cathodic reactions proceed at equilibrium, with K^0 the standard reaction rate constant, larger values of K^0 indicating faster reactions. Finally, the overpotential at the electrode surface $\eta = \phi_{\text{elec}} - \phi_i - E_{\text{eq}}$, measures the difference between the applied potential upon passage of current, $\phi_{\text{elec}} - \phi_i$, where ϕ_{elec} is the local electronic potential at the electrode surface, and the equilibrium (i.e., zero current) potential E_{eq} . The latter, also known as open circuit voltage, is given by the Nernst equation

$$E_{\text{eq}} = \tilde{E}_0 + \frac{RT}{n_e F} \ln \left(\frac{c_O^*}{c_R^*} \right), \tag{13}$$

in terms of the reference species concentrations and the standard reversible potential \tilde{E}_0 [22].

The equilibrium potential E_{eq} is therefore a correction to the standard reversible potential (the maximum theoretical potential calculated as a function of the change of Gibbs free energy of the reactions at standard conditions), once non-standard species concentrations are considered. The overpotential η therefore accounts for the activation and concentration losses [26].

3.2. Boundary conditions

Assuming steady flow conditions, the system of equations given in (8), (9) and (11) must be supplemented with appropriate boundary conditions. At the outlet section of the flow domain $x = L$, we impose zero flux of ionic potential and species concentration

$$c_j \nabla \phi_i \cdot \mathbf{n} = 0, \quad \text{and} \quad D_j \nabla c_j \cdot \mathbf{n} = 0 \tag{14}$$

with \mathbf{n} the unit outward normal vector. Whereas at the inlet section $x = 0$, we impose zero flux of ionic potential $c_j \nabla \phi_i \cdot \mathbf{n} = 0$ and Dirichlet boundary conditions for the species concentration, yielding

$$y < h_0 \quad \Rightarrow \quad \begin{cases} c_{\text{pBQ}} = c_{\text{pBQ}}^0 (1 - \text{SoC}) \\ c_{\text{pBQ}^-} = c_{\text{pBQ}^-}^0 \text{SoC} \end{cases} \tag{15}$$

and

$$y > h_0 + \Delta h \quad \Rightarrow \quad \begin{cases} c_{\text{H}_2\text{Q}} = c_{\text{H}_2\text{Q}}^0 (1 - \text{SoC}) \\ c_{\text{pBQ}} = c_{\text{H}_2\text{Q}}^0 \text{SoC} \\ c_{\text{H}^+} = c_{\text{H}^+}^0 + 2c_{\text{H}_2\text{Q}}^0 \text{SoC}, \end{cases} \tag{16}$$

Thus, in a stationary system, the concentration of the different species at $x = 0$ depends only on the state of charge (SoC) of the battery, defined as the product-to-reactive concentration ratio $\text{SoC} = c_{\text{pBQ}}/c_{\text{H}_2\text{Q}}^0 = c_{\text{pBQ}^-}/c_{\text{pBQ}}^0$ [27]. The numerical values of the constants c_{pBQ}^0 , $c_{\text{H}_2\text{Q}}^0$ and $c_{\text{H}^+}^0$ used in the computations to be presented below are taken from [4] (see Tables 2 and 3).

The Péclet number measures the relative importance of convection with respect to upstream diffusion of the different species $Pe_i = Re(\nu_1/D_i)$. A representative example is H_2Q in the catholyte (fluid 2), with $Pe \simeq 10^4$ calculated using $D_0 = 4.10 \times 10^{-8} \text{ m}^2/\text{s}$ [4], the data included in tables 2 and 3 and the kinematic viscosity of water-based electrolytes $\nu_2 = 10^{-6} \text{ m}^2/\text{s}$. In our model, the electrochemical reactions at the electrodes are contemplated for $x > L_1$. These reactions

would induce changes in the up-stream concentration of the different species in a region of characteristic length l as a consequence of streamwise diffusion. The order of magnitude of this region l can be estimated by assuming that convective $c_{i,0}\bar{u}_1$ and axial diffusion terms $D_j c_{i,0}/l$ are of the same order of magnitude in Eq. (9), yielding the scaling $l/L \sim (PeL/h)^{-1}$. From this expression we can easily check that large values of Pe indicate that the upstream influence of the electrochemical reactions on the species concentration is constrained to a small region $l \ll L$. Therefore, its effect can be neglected in the first approximation and the utilization of uniform species concentration in the boundary conditions at $x = 0$ specified before in (16) is justified.

At the electrode surfaces $y = (0, h)$, $L_1 < x < L$, Faraday's law relates the molar fluxes with the electrochemical reaction rates

$$\mathbf{N}_j \cdot \mathbf{n} = \pm s_j j / (n_e F), \tag{17}$$

with s_j the stoichiometric coefficient for species j in the electrode reaction, and $n_e = (1, 2)$ the number of electrons transferred in the reaction at the negative and positive electrodes $y = (0, h)$, respectively. Note that the sign in the right hand side of (17) indicates whether species j is being consumed (-) or produced (+).

Regarding the boundary conditions for the electronic potential, we impose zero voltage at the negative current collector [28], so ϕ_{elec} is equal to the cell voltage V_{cell} at the positive current collector. Then, the overpotentials are determined as $\eta_1 = -\phi_i$ at the negative electrode, $y = 0$, and $\eta_2 = V_{cell} - \phi_i - E_{eq,T}$ at the positive electrode, $y = h$, where

$$E_{eq,T} = E_{eq,2} - E_{eq,1} = E_0 + \frac{3RT}{2F} \ln \left[\frac{SoC}{1 - SoC} \right] \tag{18}$$

represents the global equilibrium voltage of the cell [4] and $E_0 = \tilde{E}_{0,2} - \tilde{E}_{0,1} = 1.4$ V is the standard cell potential. From here on, positive electrode variables and properties are denoted by the subscript 2, while subscript 1 is used for the negative electrode. During our calculations, we set the cell potential V_{cell} to compute the current through the current collectors $j(x)$. The average current is then calculated as $I_{app} = \int_0^L j(x) d(x/L)$. Therefore, the conservation of charge at the electrodes reduces to

$$\phi_{elec,1} = 0 \text{ at } y = 0 \text{ and } \phi_{elec,2} = V_{cell} \text{ at } y = h, \tag{19}$$

At the interface, we impose continuity of species concentration and molar flux,

$$c_{j,1} = c_{j,2} \text{ and } \mathbf{N}_{j,1} = \mathbf{N}_{j,2}. \tag{20}$$

In addition, we impose continuity of current density and ionic potential,

$$\phi_{i,1} = \phi_{i,2} \text{ and } \mathbf{i}_1 = \mathbf{i}_2, \tag{21}$$

The numerical solution of the system (8), (9) and (11) with the boundary conditions (14)-(19) is obtained using a continuation method that is initiated by imposing $\phi_{elec,2} = E_{eq,T}$, $\phi_{elec,1}^0 = 0$, $\phi_i^0 = \eta_1^0 = \eta_2^0 = 0$ what gives an initially small current density $I_{app} \simeq 0$. The initial solution is then continued by slowly increasing (charge) or decreasing (discharge) $\phi_{elec,2}$ until the final stationary result corresponding to the desired value of $\phi_{elec,2} = V_{cell}$ is obtained. For each value of V_{cell} , an iterative Newton's method is used to solve the algebraic system of equations. The iteration continues until the weighted Euclidean norm of the error vector falls below 10^{-6} .

4. Numerical results

This section is devoted to describe the results of the numerical simulations of the membrane-less flow battery. As we did before with the fluid mechanics problem, we checked the independence of the electrochemical results with the grid, quantifying the computed limiting current density j_{lim} by increasing the density of the mesh, giving $j_{lim} = (3.483, 3.464, 3.470, 3.471, 3.472)$ mA/cm² for $n/n_0 = (0.29, 0.4, 0.81, 1, 1.81)$ and $V_{cell} = 0.1$ V. The value $n = n_0$ with minimum element size $\Delta\xi/h = 0.003$ was maintained in all the results shown below.

In this section we dedicated special attention to the influence of the state of charge (SoC) and the Reynolds number on the performance of the cell operating both in discharge, $V_{cell} < E_{eq,T}$, and charge, $V_{cell} > E_{eq,T}$, modes. Apart from the effect on the flow velocities discussed in Appendix A, the Reynolds number has a significant effect on the transport of active species in the electrolytes. Once the viscosity and mass diffusivities of the different species are fixed, larger flow velocities imply larger Re and Pe , what directly affects the overpotential distribution along the electrodes, the limiting current densities and the polarization curves.

4.1. Influence of the state of charge (SoC)

The state of charge (SoC) measures how much charge is left in the battery. Its influence on the overall cell voltage during discharge, $V_{cell} < E_{eq,T}$, is shown on the left plot of Fig. 2 for two representative current densities I_{app} . To calculate this figure, the applied voltage is modified so that the average current densities remain constant and equal to $I_{app} = 0.25$ and $I_{app} = 1$ mA/cm². As expected, the overall voltage increases smoothly with the state of charge except at small SoC, when the cell voltage undergoes a swift variation as a consequence of $p\text{BQ}^-$ depletion at the negative electrode $y = 0$ as illustrated

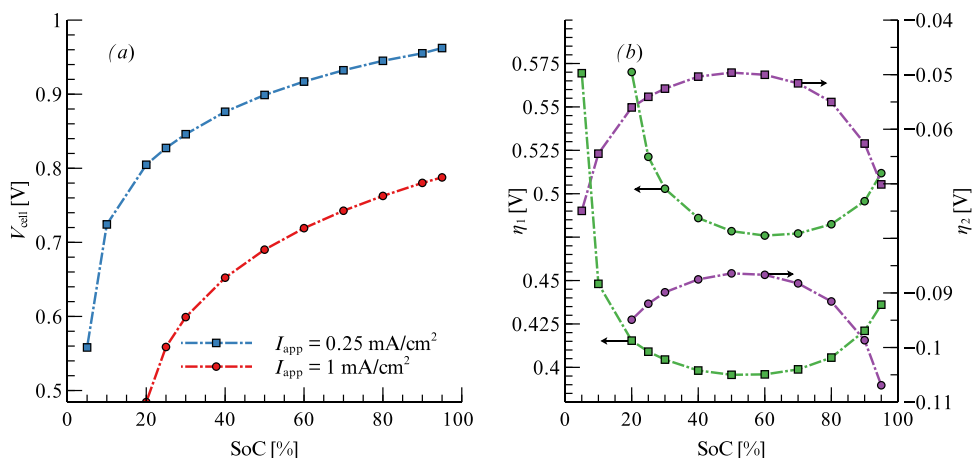


Fig. 2. (a) Variation of the applied cell voltage and (b) the negative (η_1) and positive (η_2) electrode overpotentials with SoC during the discharge of the membrane-less RFB. During our calculations, the applied voltage V_{cell} is varied to ensure constant average current densities at the electrodes $I_{app} = 0.25$ mA/cm² (\square) and $I_{app} = 1$ mA/cm² (\circ), simulating the galvanostatic operation of RFBs in experiments.

in Fig. 3 for SoC = 0.05 and $V_{cell} = 0.56$ V. Slight increments in SoC avoid the depletion of the charged ion pBQ^- near the anode electrode, which results in a rapid drop of the negative overpotential and a swift growth of the cell voltage at small SoC to maintain the current densities constant.

Indeed, the variation of the anode overpotential η_1 with the State of Charge, depicted in the right plot of Fig. 2 for $I_{app} = 0.25$ mA/cm² and $I_{app} = 1$ mA/cm², shows a sudden increase in η_1 at low SoC that is closely related to the above-mentioned reactant depletion effect. To satisfy Eq. (12) while keeping the anode current density constant, the overpotential increases as the concentration of pBQ^- becomes small. The variation of the absolute values of the negative and positive electrode overpotentials is more gradual near SoC = 1, and only small increments in the cell voltage are needed to keep the current density constant, as observed in Fig. 2. This trend agrees well with the results obtained previously for vanadium RFBs (e.g., [27]).

Illustrative concentration density plots of pBQ and pBQ^- of the cell in discharge mode are plotted in Fig. 3 for $Re = 10$, SoC = 0.05, $V_{cell} = 0.56$ V and $I_{app} = 0.25$ mA/cm². Reactant depletion is clearly observed near the negative electrode $y = 0$, where the strong gradient of pBQ^- concentration hampers the normal operation of the battery. Reducing the gradient of the active species near the electrodes is therefore crucial to achieve higher current and power densities, the small diffusivity of the active species being the most limiting factor affecting overall cell performance at low SoC conditions. To assess the effect of the species diffusivity in the results, and considering $D_{pBQ^-}^0 = 8.64 \times 10^{-8}$ m²/s as the baseline case, Fig. 4 shows the polarization curves V_{cell} vs. I_{app} computed with $D_{pBQ^-} = (0.1, 1, 10)D_{pBQ^-}^0$. As shown in the figure, the overall performance of the cell improves as D_{pBQ^-} is increased, giving, in particular, significantly higher limiting currents as a consequence of the enhanced availability of active species near the electrode due to the faster diffusion of pBQ^- .

As previously discussed, during charge an external voltage $V_{cell} > E_{eq,T}$ is applied to the cell resulting in the formation of pBQ and pBQ^- at the positive and negative electrodes, respectively. The variation of the applied voltage V_{cell} with SoC is shown in Fig. 5 during the charge of the battery. As in Fig. 2, the applied voltage is modified so that the average current densities remain constant and equal to $I_{app} = 0.25$ and $I_{app} = 0.70$ mA/cm², simulating the galvanostatic operation of RFB typically used in experiments. The curve trend observed in this figure is similar to that shown before in Fig. 2, with reactant depletion found now near the negative electrode at SoC = 0.9. As shown in Fig. 3(b), it is the large gradient of pBQ near the negative electrode in fluid 1 what strongly deteriorates the cell performance in this case.

Changes in the standard rate constant K^0 appearing in the Butler-Volmer equation (12) through the exchange current density $j_0 = K^0 c_0^{1-\alpha} c_R^{\alpha}$ are also expected to affect the polarization curve to a great extent. One of the strategies that can be followed to modify K^0 is to deposit different types of inorganic materials, such as metal oxides, clays, and zeolites, can be deposited on electrode surfaces [26] to improve the reaction rate.

Fig. 6 illustrates the effect of increasing the exchange current density j_0 by increasing the standard rate constant K^0 by a factor of 10^3 . This has a strong effect on the activation polarization region, so that while the limiting current density is not substantially changed, the polarization curve exhibits much larger current densities for a given applied voltage. For the two values of the standard rate constant considered $K = K^0$ and $K = 1000 \times K^0$, with the standard rate constants K^0 of the positive and negative half-cell reactions given in tables 2 and 3, the current density obtained for a given applied voltage is, for example, $I_{app} = 0.735$ and $I_{app} = 3.037$ mA/cm² for $V_{cell} = 0.75$ V during charge. The current densities $I_{app} = 0.087$ and $I_{app} = 1.466$ mA/cm² were obtained for $V_{cell} = 1.75$ V during discharge. As the change in K does not affect the ohmic resistance of the cell, the slope of the polarization curve remains almost identical for the range of applied voltages considered, with the differences only manifesting near open circuit conditions, when V_{cell} approaches E_{eq} .

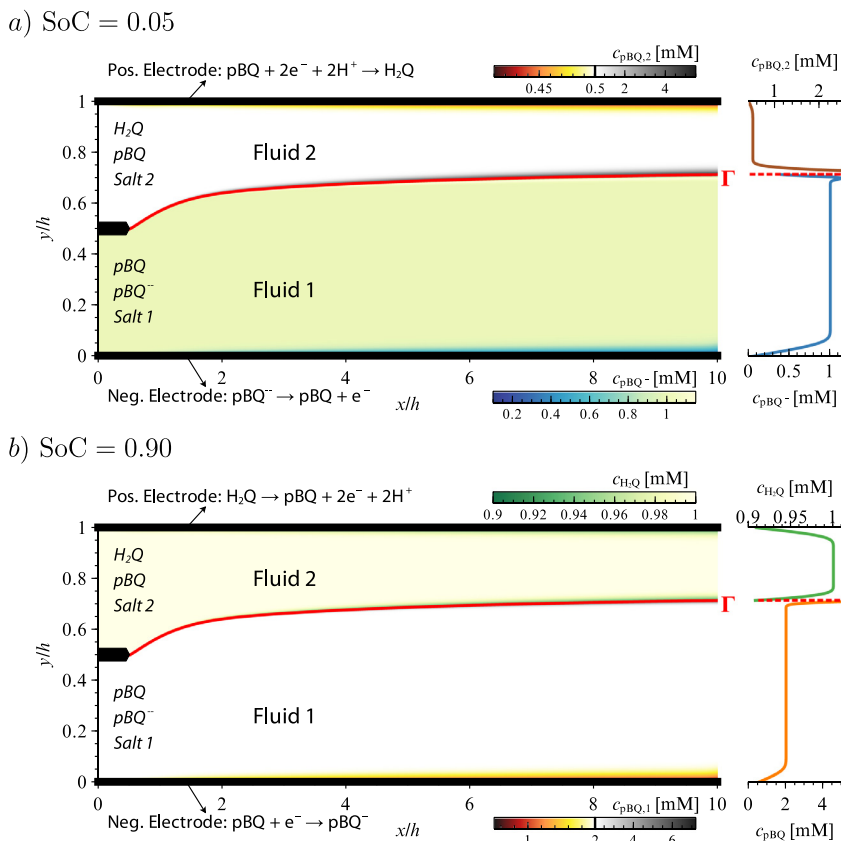


Fig. 3. a) Density plot of pBQ (catholyte $y > \Gamma$) and pBQ⁻ (anolyte $y < \Gamma$) concentration for $Re = 10$, $V_{cell} = 0.56$ V ($I_{app} = 0.25$ mA/cm²) at SoC = 0.05 during discharge operation. b) Density plot of H₂Q (anolyte $y > \Gamma$) and pBQ⁻ (catholyte $y < \Gamma$) concentration for $Re = 10$, $V_{cell} = 2.02$ V ($I_{app} = 0.25$ mA/cm²) at SoC = 0.90 during charge operation. Transverse concentration profiles of a) pBQ and pBQ⁻ and b) H₂Q and pBQ at $x = 10$ are shown in the rightmost panel of the plots.

4.2. Influence of the Reynolds number

Figs. 7 and 8 show polarization curves for SoC = 0.5 and different Reynolds numbers for the cell operating under discharge and charge modes, respectively. In the limit of low current densities (activation polarization region), the performance of the cell is independent of the flow field, the polarization curves collapsing as the applied voltage approaches the open circuit voltage. The effect of increasing both Re and Pe numbers becomes evident at small (large) applied cell voltages, concentration polarization region, when the cell operates in discharge (charge) mode. The higher concentrations of active species sustained by convection near the electrodes at larger Re prevent reactant depletion and enable the electrochemical reactions to reach higher limiting current densities. In particular, the limiting current density is seen to increase as $j_{lim} \propto Re^\alpha$, with $\alpha = 0.31$ for $V_{cell} = 0.10$ V during discharge and $\alpha = 0.32$ for $V_{cell} = 2.5$ V during charge operation, as shown in the right plots of Figs. 7 and 8, respectively. The value of α computed here is very similar to those predicted by Braff et al. [6], $\alpha = 1/3$, and Lisboa et al. [15], in a membrane-less flow battery with flow-by configuration similar to the one studied here. It is worth noting that the exponent 1/3 reported in [6] emerges theoretically in the first L ev eque problem [32] corresponding to the heat (mass) transfer problem in a developed laminar velocity profile with prescribed wall temperature (concentration), while the slightly smaller values obtained here are compatible with more complex boundary conditions [33].

Following [13], the single-pass conversion efficiency Ψ of the cell is defined as the ratio of reactant consumed at the electrode to the convective flux of reactant into the channel

$$\Psi = \frac{\int_0^L N_{pBQ}|_{y=h} \cdot \mathbf{n} \, dx}{\int_{h_0+\Delta h}^h c_{pBQ} \mathbf{v} \cdot \mathbf{n} \, dy \Big|_{x=0}} \tag{22}$$

In their boundary layer analysis, Braff et al. [13] calculated the asymptotic value of the product Ψj_{lim} obtaining a constant value for a plug-flow velocity profile and a continuous decay $\Psi j_{lim} \sim Re^{-1/3}$ for a fully-developed Poiseuille velocity pro-

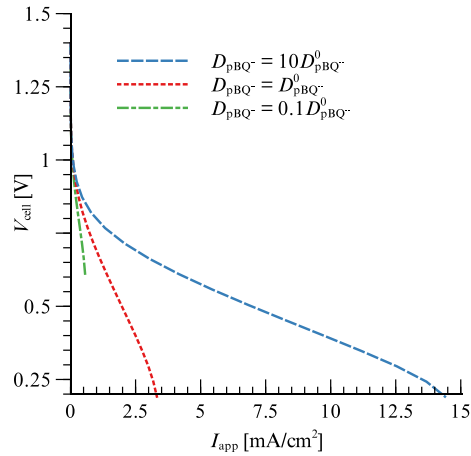


Fig. 4. Polarization curves at SoC = 0.5, $Re = 10$ for different diffusion coefficients of species as indicated in the legend, with $D_{pBQ}^0 = 8.64 \times 10^{-8} \text{ m}^2/\text{s}$ the baseline diffusion coefficient.

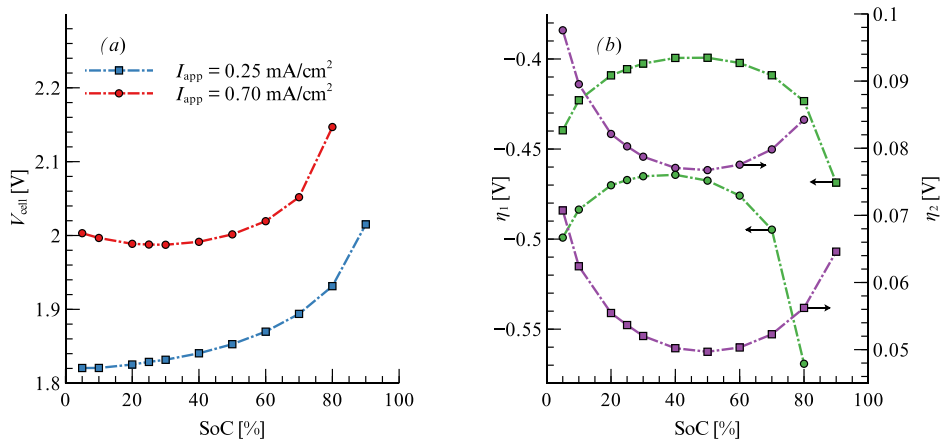


Fig. 5. (a) Variation of the cell voltage and (b) the negative (η_1) and positive (η_2) electrode overpotentials with SoC during the charge of the membrane-less RFB. During our calculations, the applied voltage V_{cell} is varied to ensure constant average current densities at the electrodes $I_{app} = 0.25 \text{ mA}/\text{cm}^2$ (\square) and $I_{app} = 0.70 \text{ mA}/\text{cm}^2$ (\circ), simulating the galvanostatic operation of RFBs in experiments..

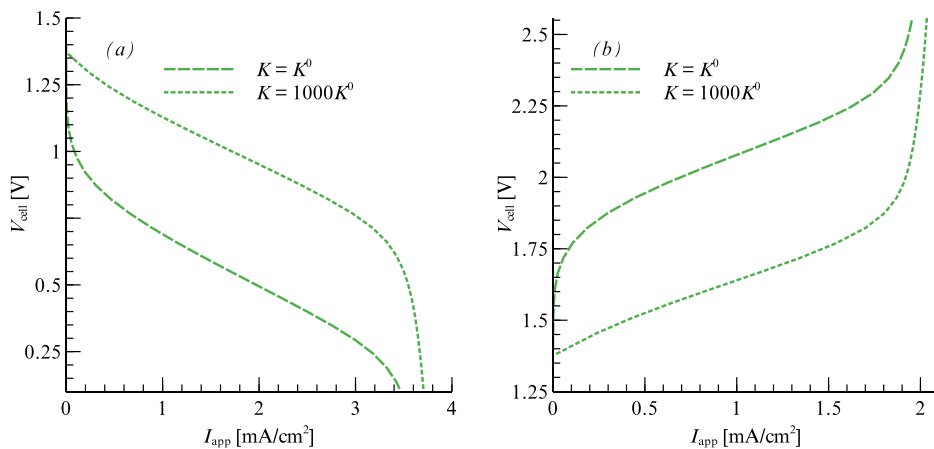


Fig. 6. Effect of the standard reaction constant (K^0) on the polarization curve for $Re = 10$, SoC = 0.5 during (a) discharge and (b) charge operation.

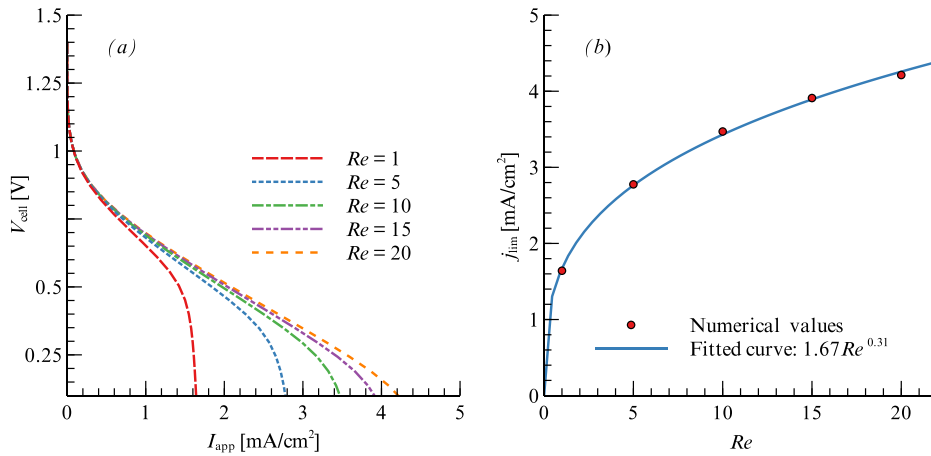


Fig. 7. (a) Discharge polarization curves for different Reynolds numbers: $Re = 1$ (red dashed line), $Re = 5$ (blue dotted line), $Re = 10$ (green dashed-dotted line), $Re = 15$ (purple dashed-dotted-dotted line), $Re = 20$ (orange dotted-fine line). (b) Variation of the limiting current density with the Reynolds number for $V_{cell} = 0.1$ V. Both figures are calculated at 50% SoC. (For interpretation of the references to colour in this figure legend, the reader is referred to the web version of this article.)

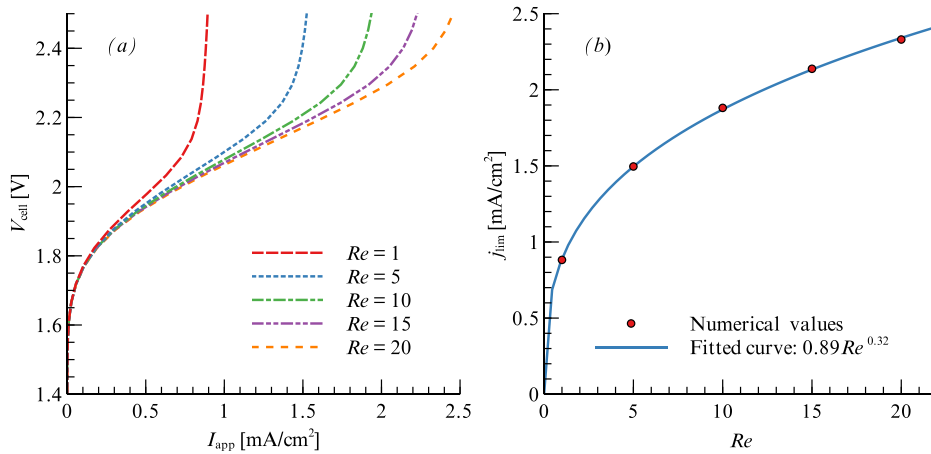


Fig. 8. (a) Charge polarization curves for different Reynolds numbers: $Re = 1$ (red dashed line), $Re = 5$ (blue dotted line), $Re = 10$ (green dashed-dotted line), $Re = 15$ (purple dashed-dotted-dotted line), $Re = 20$ (orange dotted-fine line). (b) Variation of the limiting current density with the Reynolds number for $V_{cell} = 2.5$ V. Both figures are calculated at 50% SoC. (For interpretation of the references to colour in this figure legend, the reader is referred to the web version of this article.)

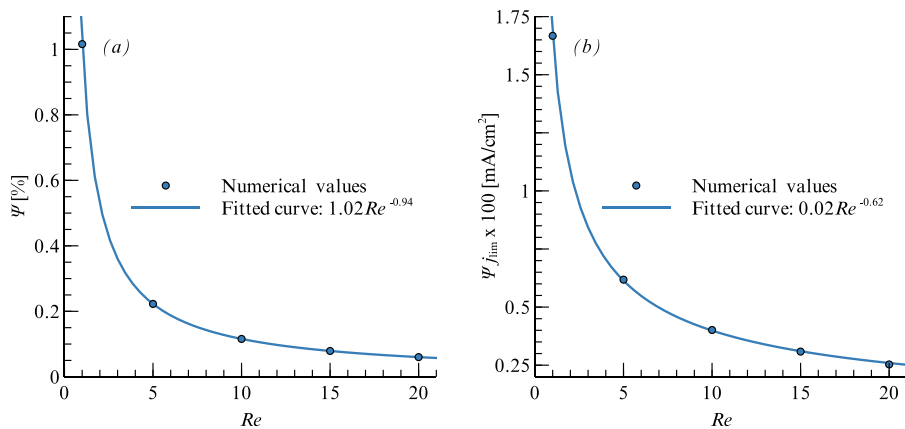


Fig. 9. (a) Variation of the single-pass conversion efficiency with Reynolds number and (b) the limiting current-single-pass conversion efficiency product with the Reynolds number for $V_{cell} = 0.70$ V at SoC = 0.5.

file. The numerical simulations carried out in this work allow the computation of the conversion efficiency Ψ plotted in Fig. 9 using the parameters included in Table 1. Our results indicate that Ψ decreases with Re in consonance with the theoretical results by [13]. However, the product Ψj_{lim} scales here as Re^λ with $\lambda = -0.62$, as shown in Fig. 9(b). The computed decay exponent is almost twice as large as that predicted theoretically by [13], which may be due to the differences between the hydrodynamic configurations of both systems. Better efficiencies are expected to occur for different values of the ratio Q_2/Q_1 .

5. Conclusions

This work constitutes the first modelling attempt that addresses both the fluid dynamical and electrochemical aspects of a membrane-less redox flow battery operated with two immiscible electrolytes. Using as input the geometrical and fluid dynamical parameters specified in Table 1 and the electrochemical parameters of Tables 2 and 3, the model is capable of computing the complex multiphase flow and then predicting the polarization curves and the concentration of the active species in both charge and discharge modes. In particular, polarization curves for different flow rates (Re) and states of charge (SoC) have been obtained in both operation modes.

On a fundamental level, at low flow rates (low Re) the membrane-less cell under study yields maximum power densities between 1 and 1.75 mW/cm² in discharge at $V_{\text{cell}} = 0.5$ V and between 1.5 and 4 mW/cm² in charge at $V_{\text{cell}} = 2$ V, comparable to the experimental proof-of-concept values reported in [4] in a quiescent flow cell. This result is fairly insensitive to changes in the flow, with maximum power densities that remain almost constant for $Re > 10$, at least in the range of parameters considered here: $Q_2/Q_1 = 1$, $\mu_2/\mu_1 = 0.0125$ and $Re \leq 20$.

During charge and discharge, the performance of the battery is limited by reactant depletion at the negative electrode. Swift changes of the applied cell voltage are necessary to keep a constant current density I_{app} when the SoC is near full charge/discharge. This is a direct consequence of the increment of the absolute values of the overpotentials induced by high gradient concentrations near the electrode. The efficiency of the battery and the maximum current density are therefore strongly dependent on the availability of reactants close to the electrodes. Our numerical tests indicate that the maximum current density increases fourfold when the diffusivity of active species pBQ^- in fluid 1 is multiplied by a factor 10.

Further improvement in the species diffusion coefficients by an appropriate engineering of the electrolytes could boost the performance of the cell. Similarly, our results show that the limiting current density increases with Re (or the Péclet number) under charge and discharge modes. In both cases, the limiting current density increases with the flow rate following the power law $j_{\text{lim}} \propto Re^\alpha$, with $\alpha \simeq 0.3$, similar to the dependence predicted by [6] and [15] using a prescribed profile for the velocity of the electrolyte.

Once demonstrated the validity of the numerical model presented here, an optimization of the fluid and geometrical parameters of the cell and the improvement of the solubility of the active molecules in the electrolyte will offer design alternatives to improve the behaviour of the cell, measured in terms of current, power and, notably, energy density.

Declaration of Competing Interest

The authors declare that they have no known competing financial interests or personal relationships that could have appeared to influence the work reported in this paper.

Acknowledgments

This work has been partially funded by the Spanish Agencia Estatal de Investigación under projects (PID2019-106740RB-I00 and PID2019-108592RB-C41/AEI/10.13039/501100011033), by Grant IND2019/AMB-17273 of the Comunidad de Madrid and by project MFreeB which have received funding from the European Research Council (ERC) under the European Union's Horizon 2020 research and innovation program (Grant Agreement No. 726217). D. Ruiz-Martín acknowledges the support of an FPI predoctoral fellowship (BES-2016-078629) under project ENE2015-68703-C2-1-R (MINECO/FEDER, UE) and the insightful conversations with professor Mark Blyth during her research visit at the University of East Anglia (UK).

Appendix A. Verification of the numerical method

To verify the numerical method, we compare in Fig. A.10 the velocity profiles computed numerically at the outlet section of the computational domain, $x = L$, with the quasi-one-directional analytical profiles obtained in the limit of very slender flows $Re h/L \ll 1$. In this limit, Eqs. (3) can be integrated to give

$$\frac{u}{\bar{u}_1} = \frac{6h_0}{h} \left[\frac{B(y/h) - (y/h)^2}{3B(\Gamma/h)^2 - 2(\Gamma/h)^3} \right], \quad y < \Gamma \quad (\text{A.1})$$

$$\frac{u}{\bar{u}_1} = \frac{6h_0}{h} \frac{1}{\mu_2/\mu_1} \left[\frac{1 - (y/h)^2 + B(y/h - 1)}{3B(\Gamma/h)^2 - 2(\Gamma/h)^3} \right], \quad y > \Gamma \quad (\text{A.2})$$

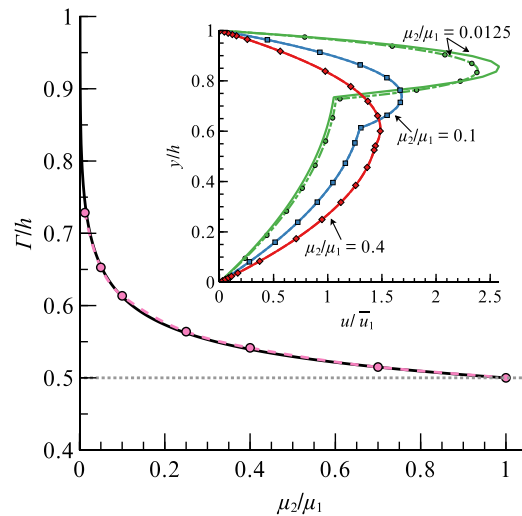


Fig. A.10. Computed (dashed lines) and asymptotic (solid lines) values of the interface location separating the electrolytes Γ/h as a function of the viscosity ratio μ_2/μ_1 . The inset depicts the velocity profiles at $x=L$ for $Re = 10$ and different values of μ_2/μ_1 . The computed velocity profiles are plotted using dashed lines while the asymptotic solution (A.1)–(A.2) are plotted using solid curves.

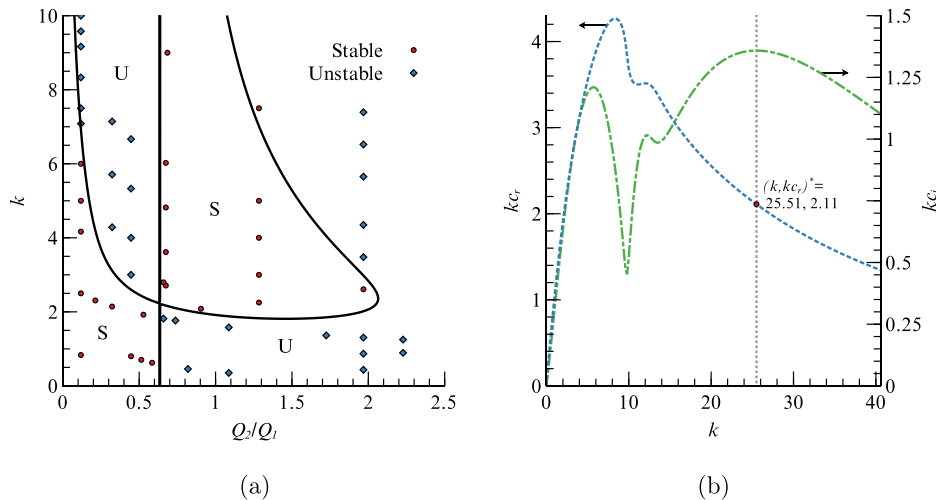


Fig. A.11. (a) Neutral stability diagram for the interfacial mode in the $(Q_2/Q_1, k)$ -plane obtained for $\mu_2/\mu_1 = 0.4$, $Re = 10$. Solid lines show the results of the linear stability carried out in [34] while markers illustrate our numerical results. (b) Variation of the real and imaginary growth rates with the wave number for the downstream unidirectional solution for $\mu_2/\mu_1 = 0.0125$, $Re = 20$.

with $B = [(1 - \mu_2/\mu_1)(\Gamma/h)^2 - 1]/[(1 - \mu_2/\mu_1)(\Gamma/h) - 1]$. The interface is then located at $y = \Gamma$ to ensure mass conservation $(Q_1 + Q_2)/Q_1 = 1 + Q_2/Q_1 = (h/h_0) \int_0^1 (u/\bar{u}_1) d(y/h)$. The velocity profiles given above in (A.1) and (A.2) are compared in Fig. A.10 with the numerical solution for a series of fluids with $\mu_2/\mu_1 = (0.1, 0.05, 0.0125)$ in a slender computational domain with length $L/h = 10$, $Re = 10$ and $Q_2/Q_1 = 1$. The match between the analytical and numerical results is very good in all cases tested except for $\mu_2/\mu_1 \ll 1$. Nevertheless, the small differences observed between the curves in Fig. A.10 in the case $\mu_2/\mu_1 = 0.0125$ disappeared when a longer computational domain was used, thus leaving enough space for the flow to become fully developed.

To further verify the numerical method, we studied the stability of the far field solution $x/L \gg 1$ associated with the discontinuity in the shear rate due to the viscosity jump across the interface [20]. To this end, we considered the most unstable condition, found when the surface tension is negligible $\sigma = 0$. To avoid the interference with shear-flow instabilities, that arise at Reynolds numbers $Re > Re_c = 27.13$ [19] and trigger the onset of turbulence, this stability analysis is carried out at $Re = 10$, well below Re_c . To do so, the base state flow given by (A.1) and (A.2) and the interface location are subjected to a normal-mode disturbance of the form

$$(\bar{u}, \bar{v}, \bar{\Gamma}) = (u, 0, \Gamma) + A(1, 1, 1) \exp[ik(x - ct)], \tag{A.3}$$

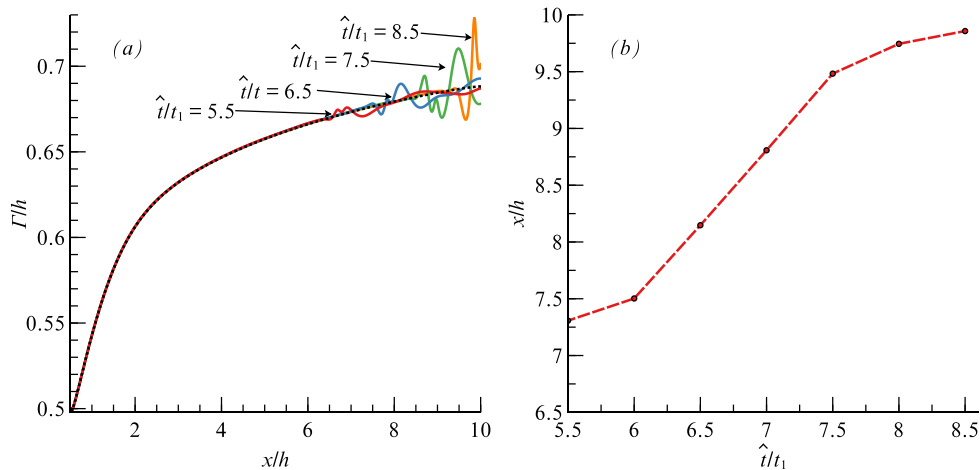


Fig. A.12. (a) Perturbed interface profiles for $\mu_2/\mu_1 = 0.0125$, $Q_2/Q_1 = 1$ and $Re = 20$ at $\hat{t}/t_1 = 5.5$ (red), $\hat{t}/t_1 = 6.5$ (blue), $\hat{t}/t_1 = 7.5$ (green) and $\hat{t}/t_1 = 8.5$ (yellow), with $t_1 = h/\hat{u}_1$ and \hat{t} is time after the perturbation has been switched off. The dotted line represents the unperturbed interface profile. (b) Evolution with time \hat{t} of the position of the maximum amplitude of the perturbation along the x axis. (For interpretation of the references to colour in this figure legend, the reader is referred to the web version of this article.)

where k and $c = c_r + ic_i$ are the wave number and phase velocity of the perturbation, with k, c_r and $c_i \in \mathcal{R}$, and $A/h \sim O(10^{-3})$ a small amplitude that ensures that the results of our computations can be compared with the linear stability analysis of Blyth and Pozrikidis [34]. The stationary solution is then unstable when $kc_i > 0$.

The results of our computations are summarized in the neutral stability diagram depicted in Fig. A.11. In this figure we compared the wavelength k that triggers an unstable behaviour of the base solution of our code with the numerical results obtained in [34] for a viscosity ratio $\mu_2/\mu_1 = 0.4$. According to Fig. A.11(a), independently of the mass flow ratio Q_2/Q_1 , there is always a range of perturbation's wave numbers that makes the solution unstable.

The nature of this instability is, however, relevant to anticipate the working behaviour of the battery. In the range of parameters considered in our study (Table 1), Valluri et al. [35] anticipated that an initially localized pulse will be amplified in a moving reference frame travelling with the perturbation but will be damped in a stationary reference frame, recovering the unperturbed solution after a sufficiently long time. To check this point, we follow the methodology presented in [35] and introduce a small-amplitude interfacial perturbation at $x = 0.7$ on the form $\Gamma + A(t)$, with A a random-phase perturbation defined as

$$A(t) = \int_0^\infty |\hat{A}(\omega_f)| e^{i[\omega_f t + \theta(\omega_f)]} d\omega_f \simeq \frac{A_0}{N_f} \sum_{j=0}^{N_f} e^{i(j\omega_{\max} t / N_f + \theta_k)} \quad (\text{A.4})$$

with $A_0 = 0.025$, $\omega_{\max} = 4.5 > 2\omega_M$, $N_f = 1500$ and the phase $0 < \theta_k < 2\pi$ generated randomly. The cut-off frequency ω_{\max} is defined as roughly twice the real frequency at which the temporal growth rate kc_i is maximum. Fig. A.11(b) illustrates the variation of the oscillation frequency kc_r and growth rate kc_i of the instability in terms of the wavelength k for $Q_2/Q_1 = 1$, $Re = 20$ and $\mu_2/\mu_1 = 0.0125$ (the potentially most unstable conditions for our battery model). This figure, in particular determines the wavelength $k = 25.51$ and frequency $\omega_M = kc_r = 2.11$ at which the growth rate is maximum.

The procedure starts by calculating a steady state solution by eliminating the time derivatives in Eq. (3). Then, the unsteady computation starts by introducing at $t = 0$ a perturbation such as the one defined in (A.4). The perturbation continues active during a few seconds before it stops and the unsteady calculations carry on describing the behaviour of the interface. The results are shown in Fig. A.12 for $Re = 20$, $\mu_2/\mu_1 = 0.0125$ and $Q_2/Q_1 = 1$. In this figure we depicted the time evolution of the interface at different times after the perturbation is shut off. The results included in this figure illustrates the convective nature of the instability as the perturbation abandons the domain through the rightmost boundary $x/h = 10$ and the interface returns to its stationary shape.

References

- [1] Z. Yang, J. Zhang, M.C.W. Kintner-Meyer, X. Lu, D. Choi, J.P. Lemmon, J. Liu, Electrochemical energy storage for green grid, *Chem. Rev.* 111 (5) (2011) 3577–3613.
- [2] M.O. Bamgbopa, S. Almheiri, H. Sun, Prospects of recently developed membraneless cell designs for redox flow batteries, *Renewable Sustainable Energy Rev.* 70 (2017) 506–518.
- [3] M. Park, J. Ryu, W. Wang, J. Cho, Material design and engineering of next-generation flow-battery technologies, *Nat. Rev. Mater.* 2 (1) (2017) 16080.
- [4] P. Navalpotro, J. Palma, M. Anderson, R. Marcilla, A membrane-free redox flow battery with two immiscible redox electrolytes, *Angew. Chem. Int. Edit.* 129 (41) (2017) 12634–12639.
- [5] V. Viswanathan, A. Crawford, D. Stephenson, S. Kim, W. Wang, B. Li, G. Coffey, E. Thomsen, G. Graff, P. Balducci, et al., Cost and performance model for redox flow batteries, *J. Power Sources* 247 (2014) 1040–1051.

- [6] W.A. Braff, M.Z. Bazant, C.R. Buie, Membrane-less hydrogen bromine flow battery, *Nat. Commun.* 4 (2013) 2346.
- [7] P. Navalpotro, J. Palma, M. Anderson, R. Marcilla, Corrigendum: a membrane-free redox flow battery with two immiscible redox electrolytes, *Angew. Chem. Int. Edit.* 57 (15) (2018) 3853.
- [8] M.O. Bamgbopa, Y. Shao-Horn, R. Hashaikeh, S. Almheiri, Cyclable membraneless redox flow batteries based on immiscible liquid electrolytes: demonstration with all-iron redox chemistry, *Electrochim. Acta* 267 (2018) 41–50.
- [9] P. Navalpotro, N. Sierra, C. Trujillo, I. Montes, J. Palma, R. Marcilla, Exploring the versatility of membrane-free battery concept using different combinations of immiscible redox electrolytes, *ACS Appl. Mater. Inter.* 10 (48) (2018) 41246–41256.
- [10] P. Navalpotro, C. Trujillo, I. Montes, C.M. Neves, J. Palma, M.G. Freire, J.A.P. Coutinho, R. Marcilla, Critical aspects of membrane-free aqueous battery based on two immiscible neutral electrolytes, *Energy Stor. Mater.* 26 (2020) 400–407.
- [11] L.F. Arenas, F.C. Walsh, C.P. de León, The importance of cell geometry and electrolyte properties to the cell potential of zn-ce hybrid flow batteries, *J Electrochem Soc* 163 (1) (2015) A5170.
- [12] W.A. Braff, C.R. Buie, Hydrogen bromine laminar flow electrochemical cell for high power and efficiency energy storage applications, *ECS Trans* 33 (39) (2011) 179.
- [13] W.A. Braff, C.R. Buie, M.Z. Bazant, Boundary layer analysis of membraneless electrochemical cells, *J. Electrochem. Soc.* 160 (11) (2013) A2056–A2063.
- [14] S.E. Ibáñez, A.E. Quintero, P.A. García-Salaberri, M. Vera, Effects of the diffusive mixing and self-discharge reactions in microfluidic membraneless vanadium redox flow batteries, *Int. J. Heat Mass Tran.* 170 (2021) 121022.
- [15] K.M. Lisboa, R.M. Cotta, On the mass transport in membraneless flow batteries with flow-by configuration, *Int J Heat Mass Transf* 122 (2018) 954–966.
- [16] K.M. Lisboa, R.M. Cotta, Analysis of the mass transport in corrugated membraneless flow batteries, *Appl Math Model* 77 (2020) 1512–1530.
- [17] COMSOL Multiphysics v. 5.5. COMSOL AB, Stockholm, Sweden URL www.comsol.com.
- [18] J. Donea, A. Huerta, J.-P. Ponthot, A. Rodríguez-Ferran, *Arbitrary Lagrangian-Eulerian Methods*, John Wiley & Sons, 2004.
- [19] S.G. Yiantsios, B.G. Higgins, Linear stability of plane poiseuille flow of two superposed fluids, *Phys. Fluids* 31 (11) (1988) 3225–3238.
- [20] C.-S. Yih, Instability due to viscosity stratification, *J. Fluid Mech.* 27 (2) (1967) 337–352.
- [21] R.F. Probstein, *Physicochemical hydrodynamics: an introduction*, John Wiley & Sons, 2005.
- [22] J. Newman, K.E. Thomas-Alyea, *Electrochemical systems*, John Wiley & Sons, 2004.
- [23] H. Bruus, *Theoretical microfluidics*, volume 18, Oxford university press Oxford, 2008.
- [24] A.Z. Weber, M.M. Mench, J.P. Meyers, P.N. Ross, J.T. Gostick, Q. Liu, Redox flow batteries: a review, *J. Appl. Electrochem.* 41 (2011) 1137–1164.
- [25] J. Sánchez-Monreal, M. Vera, P.A. García-Salaberri, Fundamentals of electrochemistry with application to direct alcohol fuel cell modeling, in: T. Taner (Ed.), *Proton exchange membrane fuel cell*, Intech, Rijeka, 2018, pp. 121–154.
- [26] A.J. Bard, L.R. Faulkner, *Electrochemical methods: fundamentals and applications*, John Wiley & Sons, 2001.
- [27] D. You, H. Zhang, J. Chen, A simple model for the vanadium redox battery, *Electrochim. Acta* 54 (2009) 6827–6836.
- [28] J. Kui, L. Xianguo, Water transport in polymer electrolyte membrane fuel cells, *Prog. Energ. Combust.* 37 (2011) 221–291.
- [29] T. Dippel, K.D. Kreuer, Proton transport mechanism in concentrated aqueous solutions and solid hydrated of acids, *Solid State Ionics* 46 (1990) 3–9.
- [30] P.M. Richardson, A.M. Voice, I.M. Ward, Pulsed-field gradient NMR self diffusion and ionic conductivity measurements for liquid electrolytes containing *liBF4* and propylene carbonate, *Electrochim. Acta* 130 (2014) 606–618.
- [31] J. Reiter, S. Jeremias, E. Paillard, M. Wintera, S. Passerini, Fluorosulfonyl-(trifluoromethanesulfonyl)imide ionic liquids with enhanced asymmetry, *Phys. Chem. Chem. Phys.* 15 (2013) 2565–2571.
- [32] A. Lévêque, Les lois de la transmission de chaleur par convection, *Ann. Mines Memories* 12–13 (1928). 201–299, 305–362, 381–415.
- [33] M. Vera, A. Liñán, Exact solution for the conjugate fluid-fluid problem in the thermal entrance region of laminar counterflow heat exchangers, *Int. J. Heat Mass Tran.* 54 (1–3) (2011) 490–499.
- [34] M.G. Blyth, C. Pozrikidis, Effect of inertia on the marangoni instability of two-layer channel flow, part II: normal-mode analysis, *J. Eng. Math.* 50 (2004) 329–341.
- [35] P. Valluri, L.O. Naraigh, H. Ding, P. Spelt, Linear and nonlinear spatio-temporal instability in laminar two-layer flows, *J. Fluid Mech.* 656 (2010) 458–480.